International Journal of Fatigue 153 (2021) 106501

Contents lists available at ScienceDirect

International Journal of Fatigue

journal homepage: www.elsevier.com/locate/ijfatigue

Towards a general damage law for interior micro-defect induced fatigue cracking in martensitic steels

Gang Zhu, Ya-Chun Wu, Ming-Liang Zhu *, Fu-Zhen Xuan *

Key Laboratory of Pressure Systems and Safety, Ministry of Education, School of Mechanical and Power Engineering, East China University of Science and Technology, Shanghai 200237, China

ARTICLE INFO

Keywords:
Very high cycle fatigue
Micro-defects
Fine granular area
Microstructure-hydrogen interaction
Lath martensites microstructure

ABSTRACT

Axially loaded cyclic tests of a precipitation-hardened martensitic steel at different stress ratios in 3% NaCl solution and steam environment were conducted up to very high cycle fatigue regime. In-depth fracture surface observation, quantitative characterization of microstructural damage, and theoretical modeling were carried out to illustrate the physics and mechanics of micro-defect induced interior cracking. Results showed apparent environmental effect on fatigue strength and crack initiation morphology. The fine granular area was observed for the first time in environmental media, heterogeneously distributed around micro-defect, and was found dependent on local fracture mode with a less probability in the case of faceted failure. The formation of fine granular area was confirmed as a result of microstructural damage with significant contribution from cyclic stress amplitude, and could be assisted by hydrogen speeding up lath martensites breakdown. *A chemo-mechanical model of interior cracking* was finally established based on the concept of interaction of inclusion, matrix, and environment induced plasticity. All these underpin a general fatigue damage law in micro-defects assessment for long-life structural integrity.

1. Introduction

Defects in engineering materials can be in the form of non-metallic inclusions, pores or defective microstructures related with metallurgy, un-welded areas, undercuts, surface roughness or microcracks due to manufacturing, and micro-geometric flaws such as dents, scratches, corrosion pits and others in service or maintenance [1]. Micro-defects are potential cracking sites especially in the case of fatigue loading [2], where cracks are often inevitably initiated [3]. This necessitates defect-tolerant concept in design and manufacturing, and several code and standards have been developed for structural safety assessment. Nevertheless, understanding the physics of micro-defect induced fatigue cracking has profound engineering significance in metallurgical and manufacturing processes, and can pave the way to the advancement of design against fatigue.

During the past two decades, the increasing research interest very high cycle fatigue (VHCF) of engineering materials enhances the fundamentals of micro-defect induced cracking. It has been widely accepted that crack initiation induced by internal micro-defect occupies more than 90% of fatigue life [4,5], and is often associated with microstructure-defect interaction [6–8]. The concept of matrix-defect interaction has promoted the understanding of fatigue cracking in terms of microscale defect or crack characteristics [9,10], crack nucleation and early propagation behavior [11,12], competing failure assessment method [13,14], and life prediction models [15,16]. Consequently, a series of mechanistic models for fine granular area (FGA) formation [17–21], also called optical dark area (ODA) [17] or granular bright facet (GBF) [22], have been proposed based on fracture surface observation on post-mortem specimens. This includes the earlier ones "hydrogen embrittlement assisted cracking" [23], "polygonization and micro-debonding" [24], and "dispersive decohesion of spherical carbide" [22], followed by grain refinement [25], nano-crystallization [9,26], numerous cyclic pressing [26,27]. In addition, Zhu et al. [15] revealed the early interior cracking was essentially a fatigue damage of microstructures due to inclusion-microstructure interaction induced plasticity, and proposed the "fragmentation of martensitic laths and formation of dislocation cells" model.

Nevertheless, all the above mechanistic models need verification and extension in case of fatigue cracking in extreme environment in which mechanical and chemical factors are coupled for fatigue failure. The VHCF damage of nickel-based superalloy has attracted great interests. Stinville et al. [28] thought VHCF damage at high temperature was

* Corresponding authors.
E-mail addresses: mlzhu@ecust.edu.cn (M.-L. Zhu), fzxuan@ecust.edu.cn (F.-Z. Xuan).

https://doi.org/10.1016/j.ijfatigue.2021.106501
Received 4 July 2021; Received in revised form 11 August 2021; Accepted 14 August 2021
Available online 19 August 2021

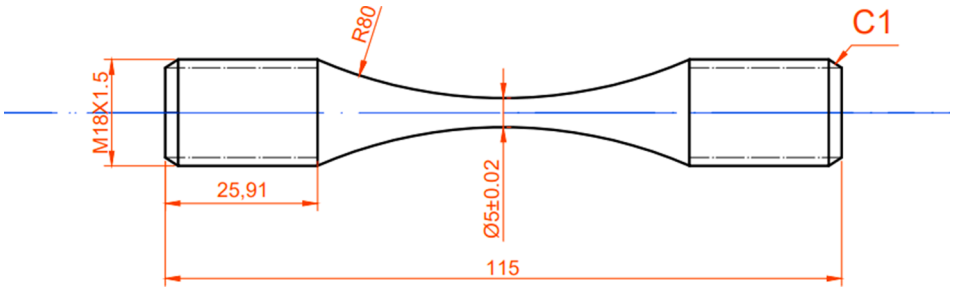

Fig. 1. The shape and dimensions of fatigue specimen (unit in mm).

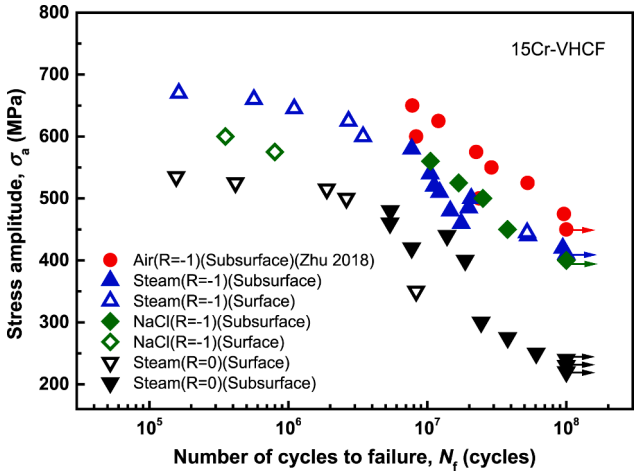

Fig. 2. *S-N* curves at various environmental conditions.

assosiated with microstructure-oxide interaction behavior for nickel-based superalloy. Cervellon et al. [29,30] reported a rough zone around fatigue crack initiation site on the fracture surface in single-crystal superalloys at 1000 °C, and correlated with localized and severe plastic activity. In another Ni-based supperalloy, Li et al. [29,30] concluded that interior fatigue failure with longer life was greatly promoted at 650 °C, which was induced from crystallographic facets associated with grain structure. Furthermore, the VHCF behavior under environment media is also an important aspect. Qian et al. [31] reported a remarkably degraded fatigue strength of a structural steel in 3.5% NaCl solution than that in air, and cracks were originated at multiple surface initiation sites with intergranular mode. Murakami et al. [23] reported that local chemical modifications could occur around an non-metallic inclusion, and internal cracking process could be enhanced by hydrogen. To the authors' knowledge, the possibility of FGA formation and its mechanism under environmental media is still an open issue. An understanding of the environmental effect on interior micro-defect induced cracking plays a supplement role in current knowledge of VHCF. In doing so, the concept of microstructure-defect interaction needs to be extended and upgraded to microstructure-defect-environment interaction, towards for a general damage law of interior micro-defect induced fatigue cracking. In addition, Sakai et al. [32] reported the slope of *S-N* curves became extremely flat and the size of FGA decreased with the increase of stress ratio, *R*, implying strong dependence of mean stress.

Therefore, in the present work, fatigue tests using specimens of a precipitation-hardened stainless steel 15Cr, the same to the one reported in our previous work [15], were carried out up to the VHCF regime in steam and 3% NaCl solution at different stress ratios. Multiscale fractographic analysis was performed using a combination of SEM, TEM, and Transmission Kikuchi diffraction (TKD) techniques. In particular, TEM diffraction/imaging and TKD techniques were used for in-depth

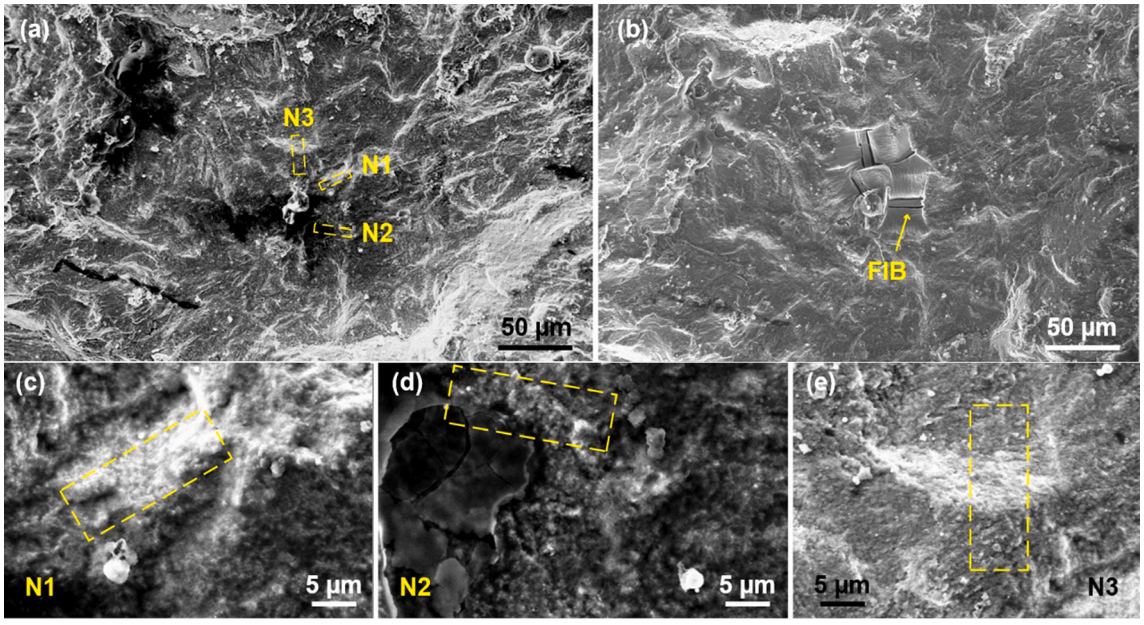

Fig. 3. Areas of interest on fracture surface of specimen in 3% NaCl at $R = -1$ ($\sigma_a = 525$ MPa, $N_f = 1.68 \times 10^7$ cycles): (a) full view of fracture surface containing micro-defect; (b) SEM image showing FIBed zones; (c-e) are enlarged views of dashed rectangular areas of N1, N2 and N3 in (a), respectively.

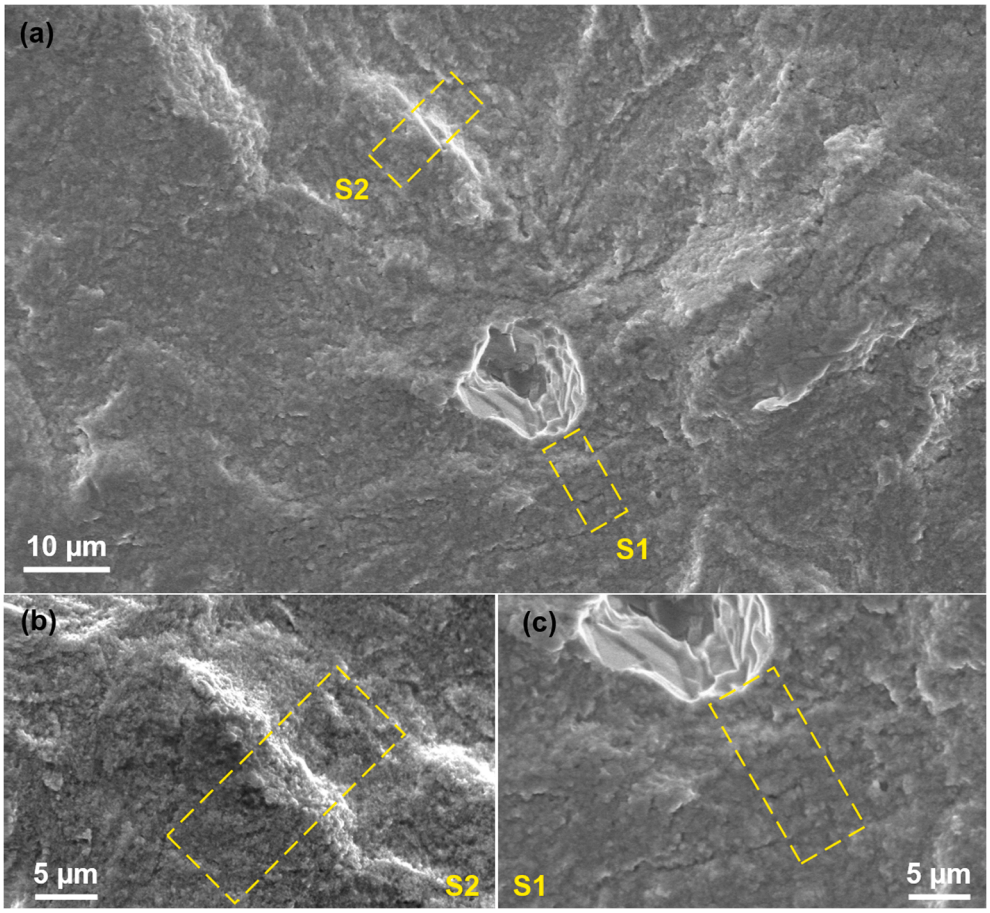

Fig. 4. Areas of interest on fracture surface of fatigued specimen in steam at $R = -1$ ($\sigma_a = 520$ MPa, $N_f = 1.12 \times 10^7$ cycles): (a) SEM image of the fracture surface; (b-c) are enlarged views of dashed rectangular areas in (a) respectively.

characterization of the microstructures and dislocation characteristics beneath the FGA features. The multiscale analysis methodology made it possible to interpret the mechanisms of damage law of lath martensitic steel in the context of interior micro-defects included fatigue cracking.

2. Materials and experiments

2.1. Materials

The material investigated in this work is a precipitation-hardened stainless steel, whose chemical compositions (wt.%) include: C 0.029%, S 0.001%, P 0.017%, Cr 14.47%, Si 0.43%, Mn 0.46%, Ni 6.29%, Cu 1.46%, Mo 0.88% and Fe the balance. The steel was water quenched at 1030 ℃ for 1.5 h, followed by a thermal aging treatment at 482 ℃ for 4 h with air cooling, and the prior austenite grain size is in the range 25–35 μm. The microstructures are mainly lathy martensite with little austenite [15].

2.2. Experiments

Fatigue specimens were machined into the shape and dimensions as shown in Fig. 1, according to ASTM E466. Prior to fatigue testing, the residual stress and surface roughness were measured by Proto-I XRD X-ray diffractometer and Alicona IFMG4 three-dimensional topography, respectively. The residual stress was measured by using Cr target, at a voltage of 20 kV, tube current of 4 mA, diffraction surface of (211), selected 2θ of 153°-161°, with a scanning speed of 0.6°/min. The R_a of all fatigue specimens are below 0.3 μm.

Fatigue tests were conducted on electromagnetic resonance machine at a frequency around 120 Hz under steam and NaCl solution environments that can well represent in-service condition of steam turbine blade. The environment conditions include saturated steam at 100 ℃ with oxygen content<0.8 ppm and 3% NaCl solution at 80℃. Loading level was carefully selected to have the data points mainly located in the HCF and VHCF regimes in a *S-N* curve plot. Cycling up to longer lifetime, i.e., 5×10^8 cycles, was preferred but it would be more time-consuming for testing at such range of loading frequency. As a result, each test was stopped until the specimen was broken or fatigue lifetime reached 10^8 cycles. Note that the R is -1 for testing at NaCl solution, and R values are -1 and 0 in steam.

Fatigue fracture surface of all failed specimens were examined with the help of Scanning Electron Microscope (SEM, EVO MA15, Zeiss, Germany). In addition, neighboring areas around inclusion on fracture surfaces with FGA morphology were firstly milled by Focused Ion Beam (FIB, Cross Beam 540, Zeiss, Germany) into thin film samples, followed by Transmission Electron Microscopy (TEM, Talos F200S, Thermofisher, USA) for dislocation structure observation and Selective Area Diffraction (SAD) analyses. Finally, high-resolution Electron Backscatter Diffraction (EBSD, Symmetry, Oxford, UK) with Transmission Kikuchi diffraction (TKD) analysis was used for grain size/orientation mapping on the milled thin film samples with a step size of 10 nm.

The distribution of hydrogen was investigated on a few selected fracture surfaces using secondary ion mass spectroscopy in a time of-flight setup (ToF-SIMS, GAIA 3 GMU Model 2016). Specimens (3% NaCl, steam and air) taken for this examination were cyclically loaded up to 10^7 cycles that guaranteed the formation of FGA around the critical inclusion, meanwhile, the fractured specimens were stored in liquid nitrogen to avoid effusion of hydrogen from the fracture surface. The

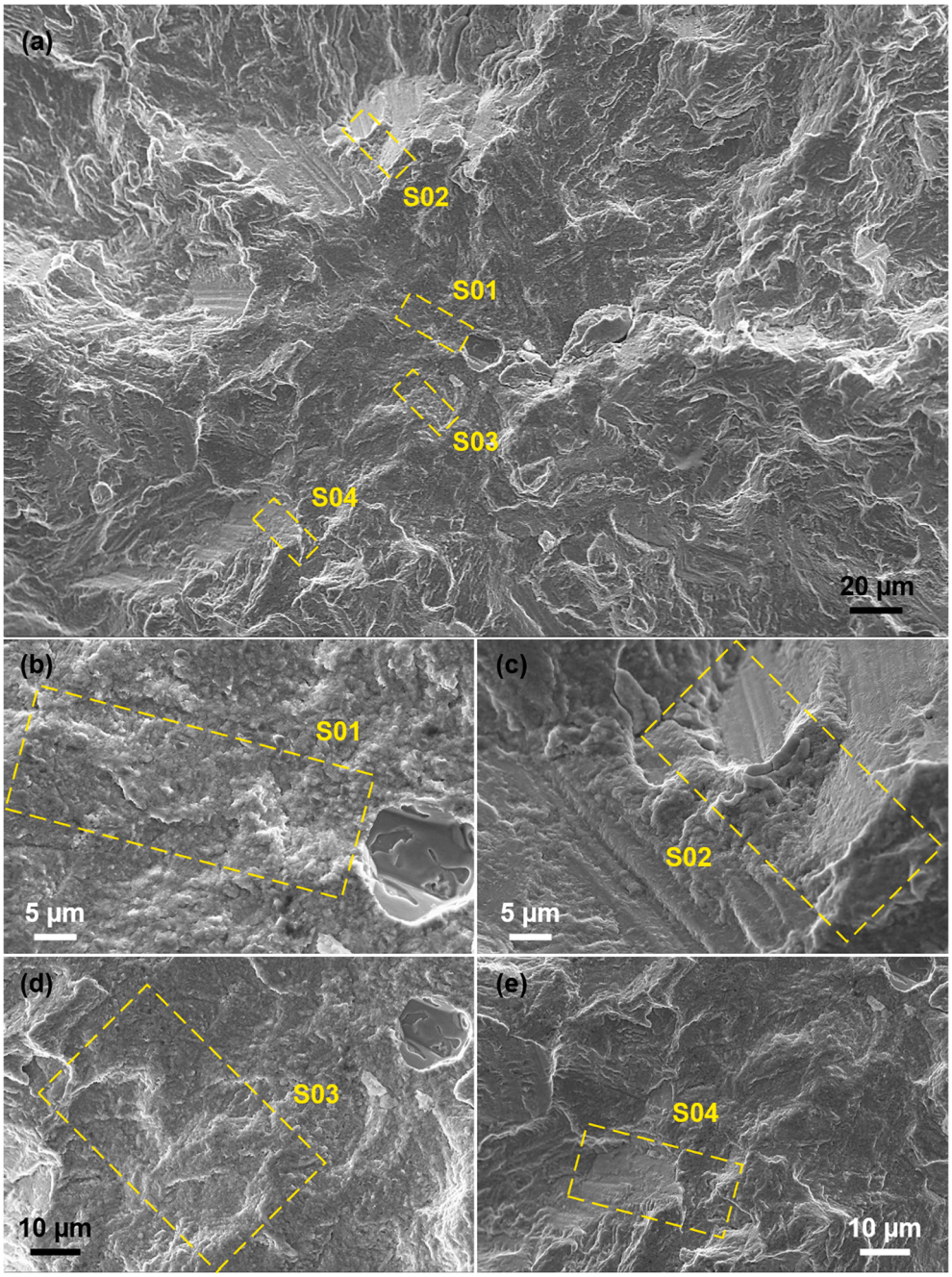

Fig. 5. Areas of interest on fracture surface of fatigued specimen in steam environment at $R = 0$ ($\sigma_a = 440$ MPa, $N_f = 1.38 \times 10^7$ cycles): (a) SEM image of the fracture surface, (b-e) are enlarged views of dashed rectangular areas of S01, S02, S03 and S04 in (a), respectively (note the S02 in (c) have facets).

fracture surface was cleaned for 100 s with 2 keV oxygen ions at a total current of −500nA, removing about 25 nm of the surface. The secondary ion beam scanned across 500 × 500 μm^2 to avoid crater edge effects on the analysis beam. It was scanned with a 15 keV Ga^+ pulsed primary ion beam at a total current of 1.5 pA about an area of 300 × 300 μm^2 around crack origin. The deposited energy during ion bombardment is sufficient to loose hydrogen from traps and accelerate its effusion, especially at a high current, high rate oxygen bombardment. The imaging itself was performed using 256×256 pixels integrating over 1000 scans for each sample. The hydrogen element was measured, and using a quantitative chemical analysis exclude matrix effects completely.

3. Results

3.1. S-N curves

Fig. 2 shows the *S-N* curves at three environment conditions. The *R* at steam are 0 and −1, and it is −1 in NaCl and air environments. Fatigue lifetime of all data is in the range of 10^5-10^8 cycles, and thus within the HCF and VHCF regimes. Runout specimens are indicated by arrows. With the stress level decreasing, the fatigue lifetime increases, meanwhile, the *S-N* curves present two-stage shape which well corresponds to surface-initiated and interior-initiated cracking mode. All the interior crack initiation is related with non-metallic inclusions. The transfer of cracking mode is also apparent when comparing slope of *S-N* curves for fatigue lifetime around 5 × 10^6 cycles. The data points of surface-

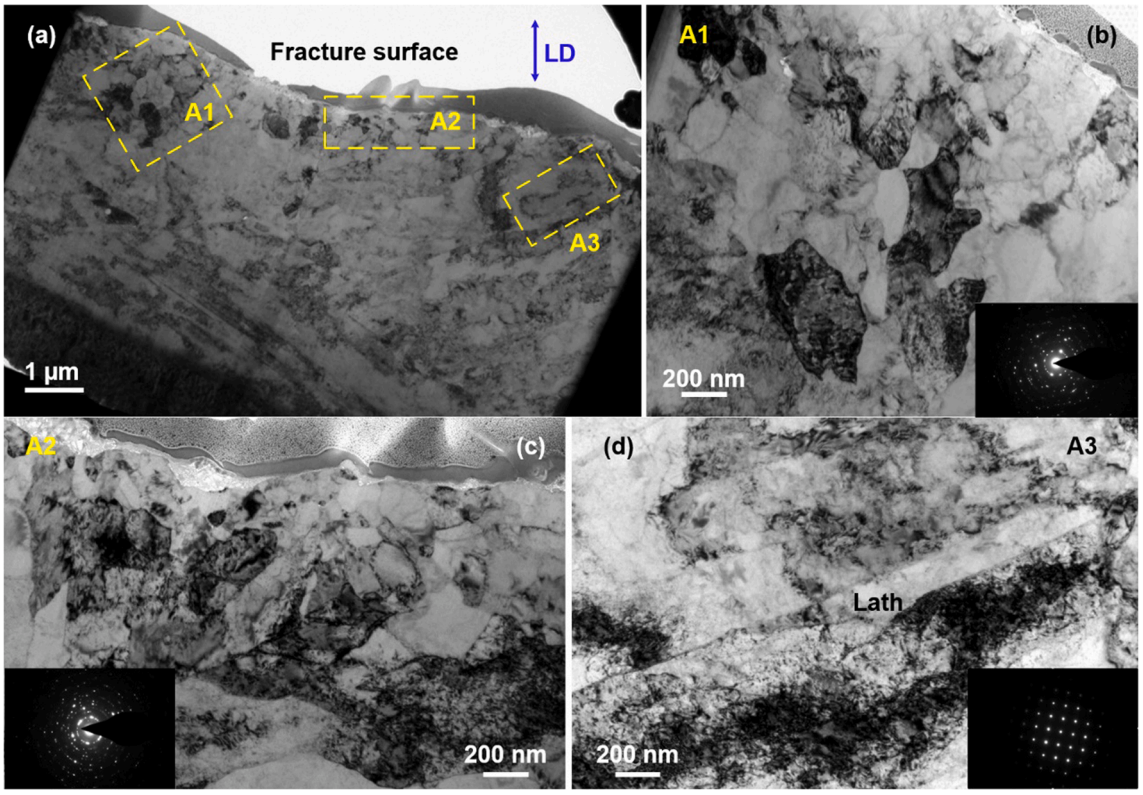

Fig. 6. TEM images showing detailed morphologies of the FIBed sample N1: (a) an overview of sub-structures below fracture surface, (b-d) are enlarged dash areas of A1, A2 and A3, while the inserted figures in (b-d) showing results by selected area diffraction technique.

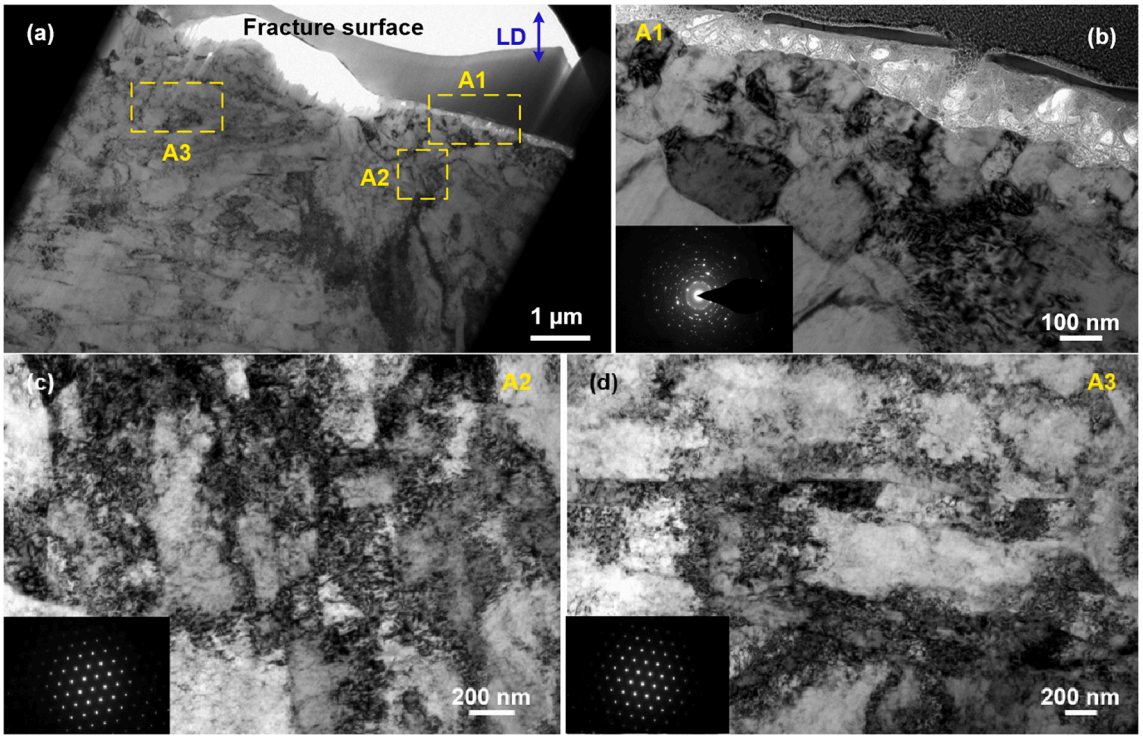

Fig. 7. TEM images showing detailed morphologies of the FIBed sample N2: (a) an overview of sub-structures below fracture surface, (b-d) are dashed areas of A1, A2 and A3, while the inserted figures in (b-d) showing results by selected area diffraction technique.

initiated failures are more dispersed than interior-initiated failures, which is probably because of environmental attack on specimen surface.

The fatigue strength at R of -1 under NaCl and steam environments are lower than that in air, which is not unexpected. As for the two environmental media, interestingly, the fatigue strength in the case of surface cracking mode is lower in NaCl environment than that in steam,

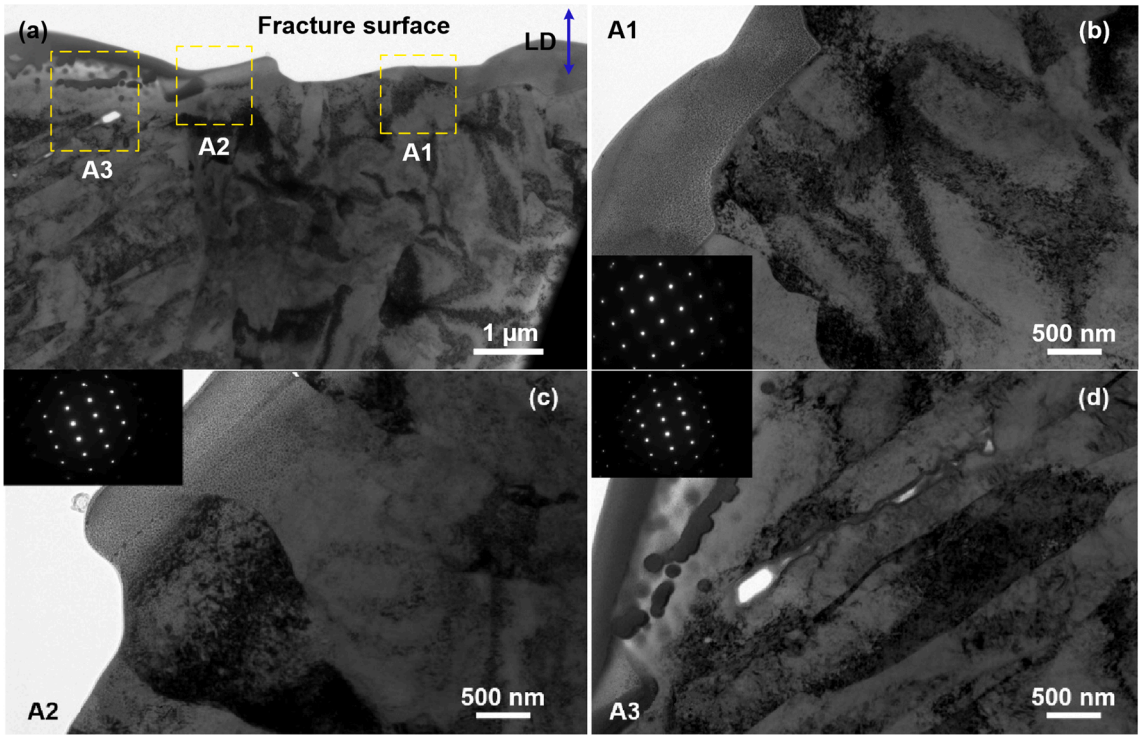

Fig. 8. TEM images showing detailed morphologies of the FIBed sample N3: (a) an overview of sub-structures below fracture surface, (b-d) are dashed areas of A1, A2 and A3, while the inserted figures in (b-d) showing results by selected area diffraction technique.

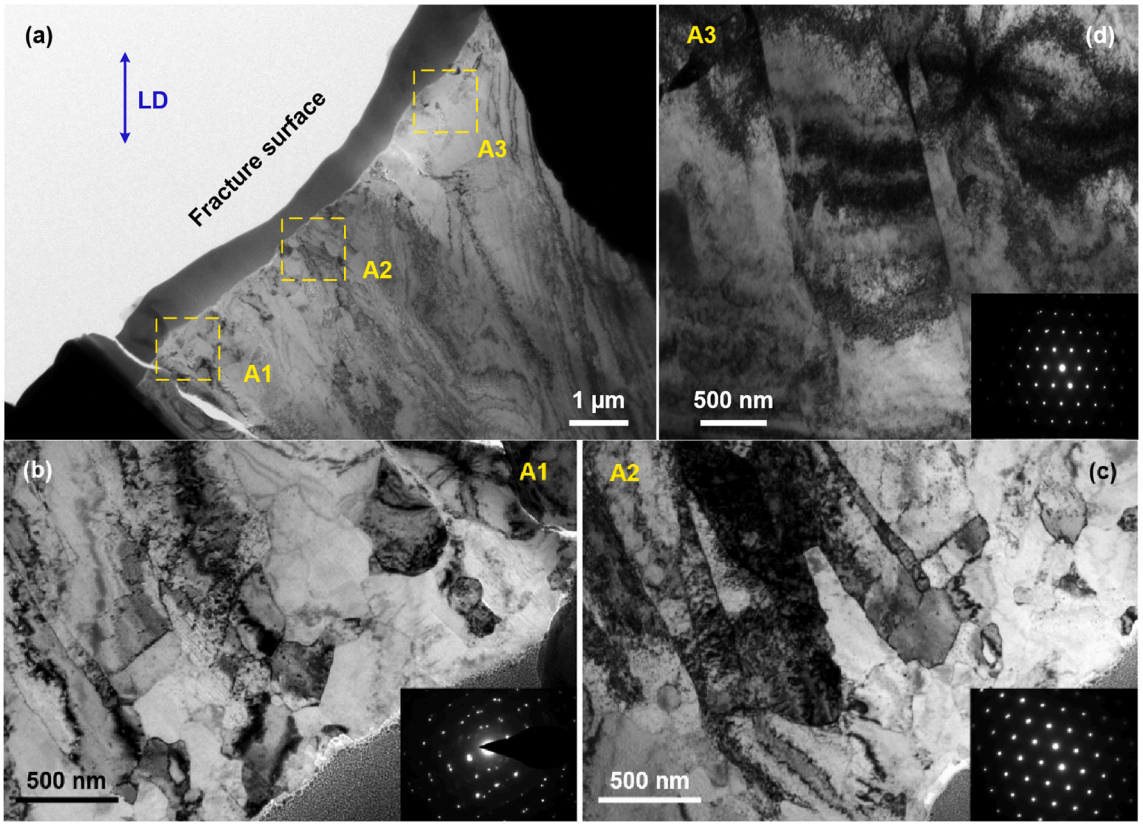

Fig. 9. TEM images showing detailed morphologies of the FIBed sample S1: (a) an overview of sub-structures below fracture surface; (b-d) are enlarged dashed areas of A1, A2 and A3, while the inserted figures in (b-d) showing results by selected area diffraction technique.

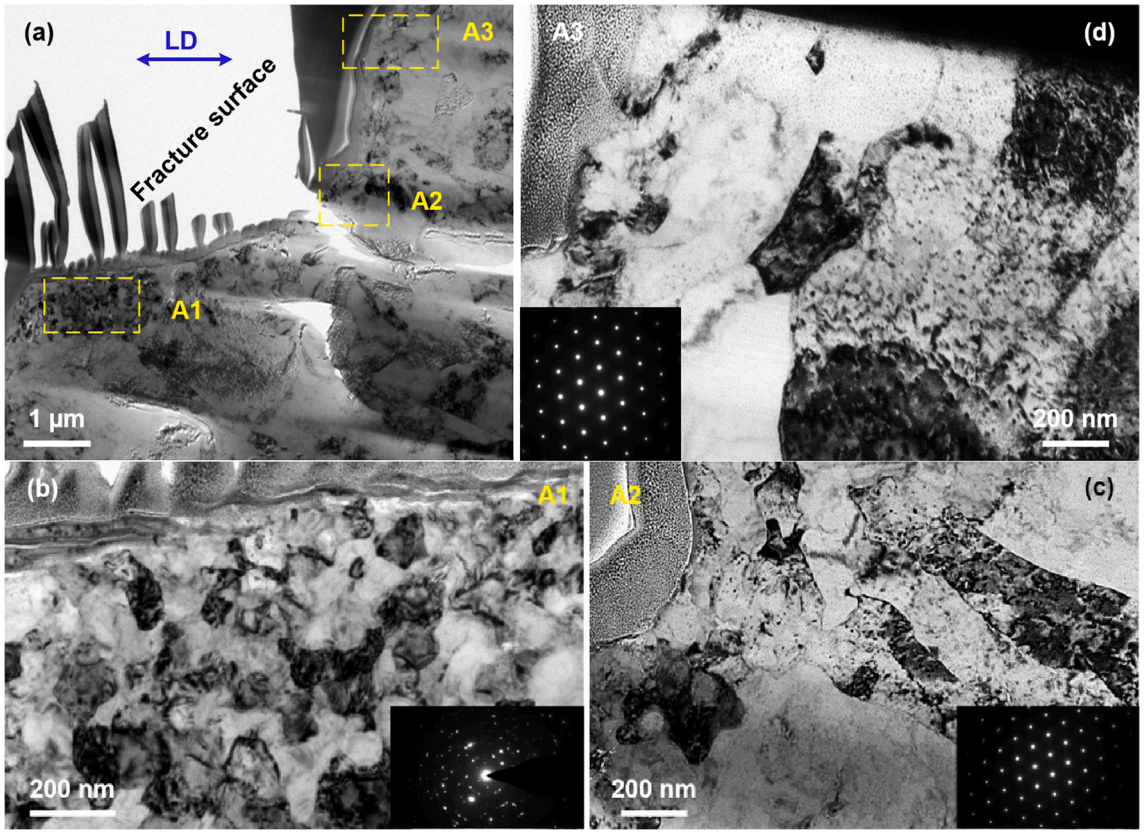

Fig. 10. TEM images showing detailed morphologies of the FIBed sample S2: (a) an overview of sub-structures below fracture surface; (b-d) are enlarged dashed areas of A1, A2 and A3, while the inserted figures in (b-d) showing results by selected area diffraction technique.

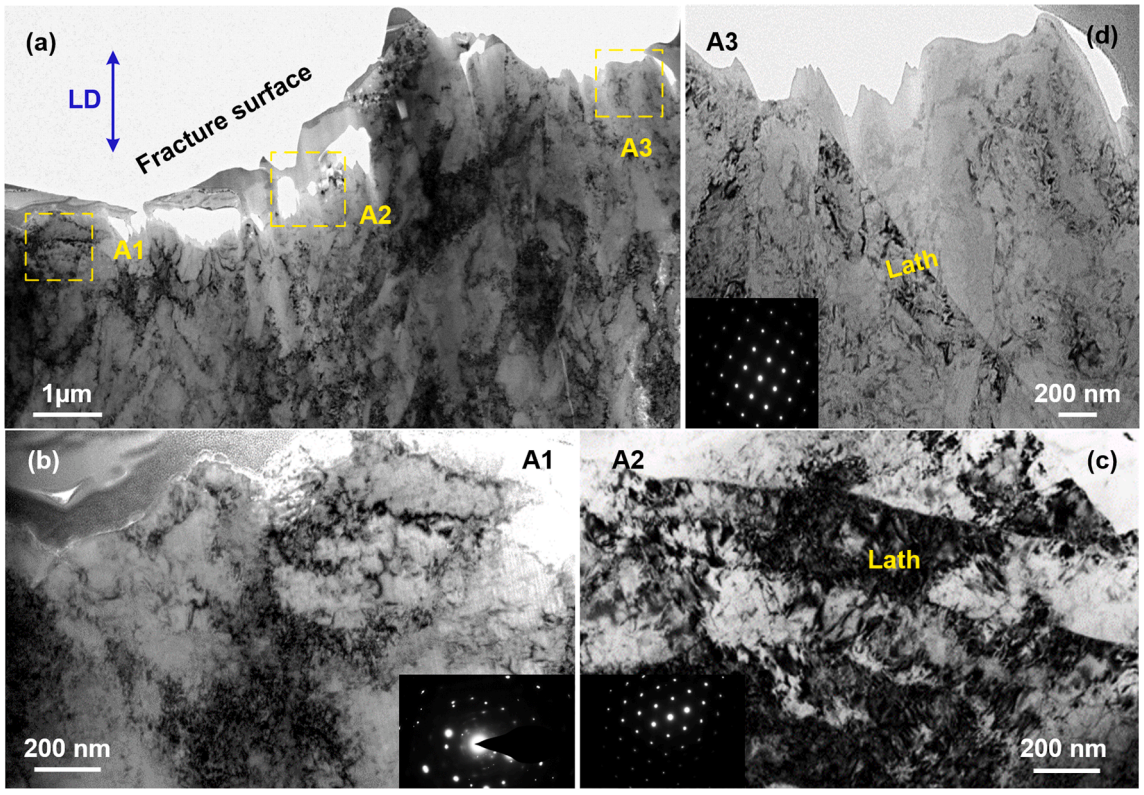

Fig. 11. TEM images showing detailed morphologies of the FIBed sample S01: (a) an overview of sub-structures below fracture surface; (b-d) are enlarged dashed areas of A1, A2 and A3, while the inserted figures in (b-d) showing results by selected area diffraction technique.

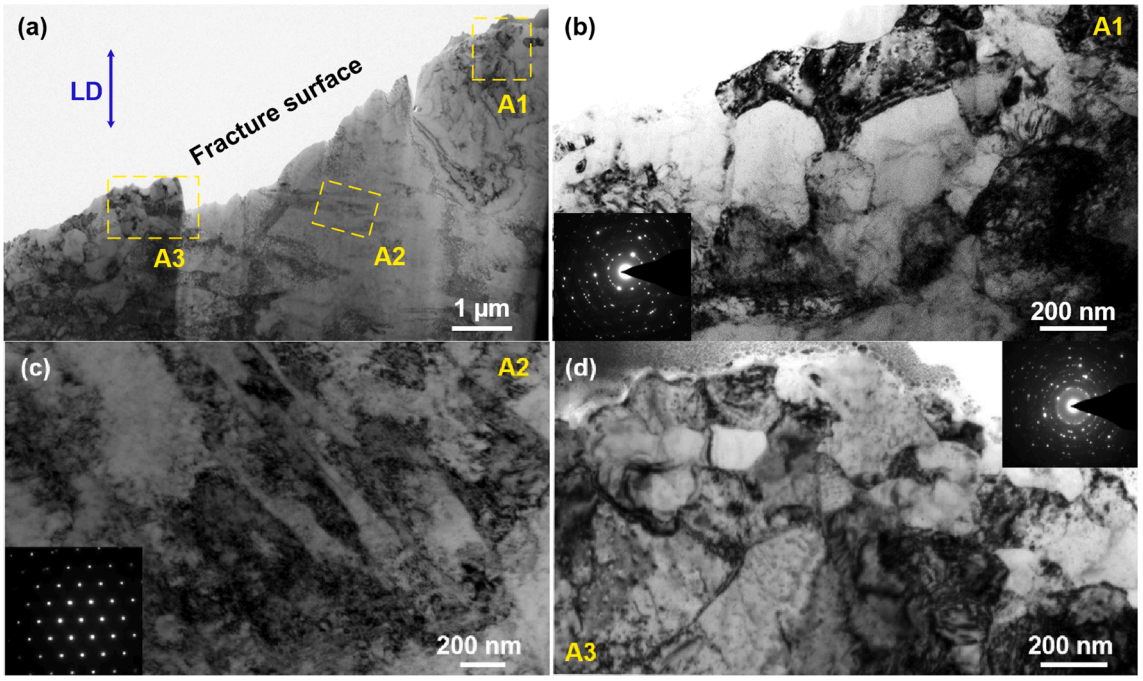

Fig. 12. TEM images showing detailed morphologies of the FIBed sample S03: (a) an overview of sub-structures below fracture surface, (b-d) are enlarged dashed areas of A1, A2 and A3, while the inserted figures in (b-d) showing results by selected area diffraction technique.

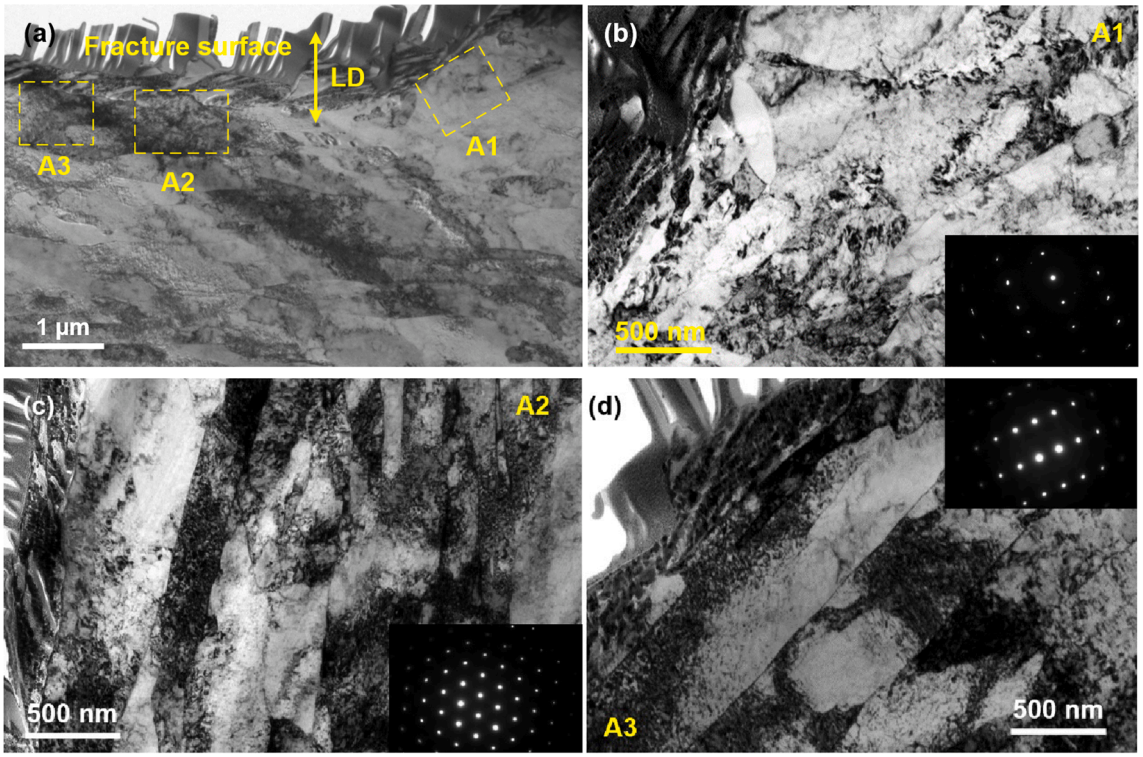

Fig. 13. TEM images showing detailed morphologies of the FIBed sample S02: (a) an overview of sub-structures below fracture surface, (b-d) are enlarged dashed areas of A1, A2 and A3, while the inserted figures in (b-d) showing results by selected area diffraction technique.

while they are comparable for interior-induced fatigue cracking. This is reasonable as the NaCl solution is more corrosive and thus easier for surface attack. It is also worth noting that, the fatigue strength in steam decreases sharply with the increasing of R from -1 to 0, while the shape of *S-N* curve is almost similar. It appears that, the slope of *S-N* curve may imply the intrinsic resistance to fatigue cracking, and the physics of index value of Basquin equation.

3.2. *Fracture surface observation*

Fatigue failure is dominated by internal micro-defects in the HCF and VHCF regimes. The typical micro-defect induced fatigue cracking

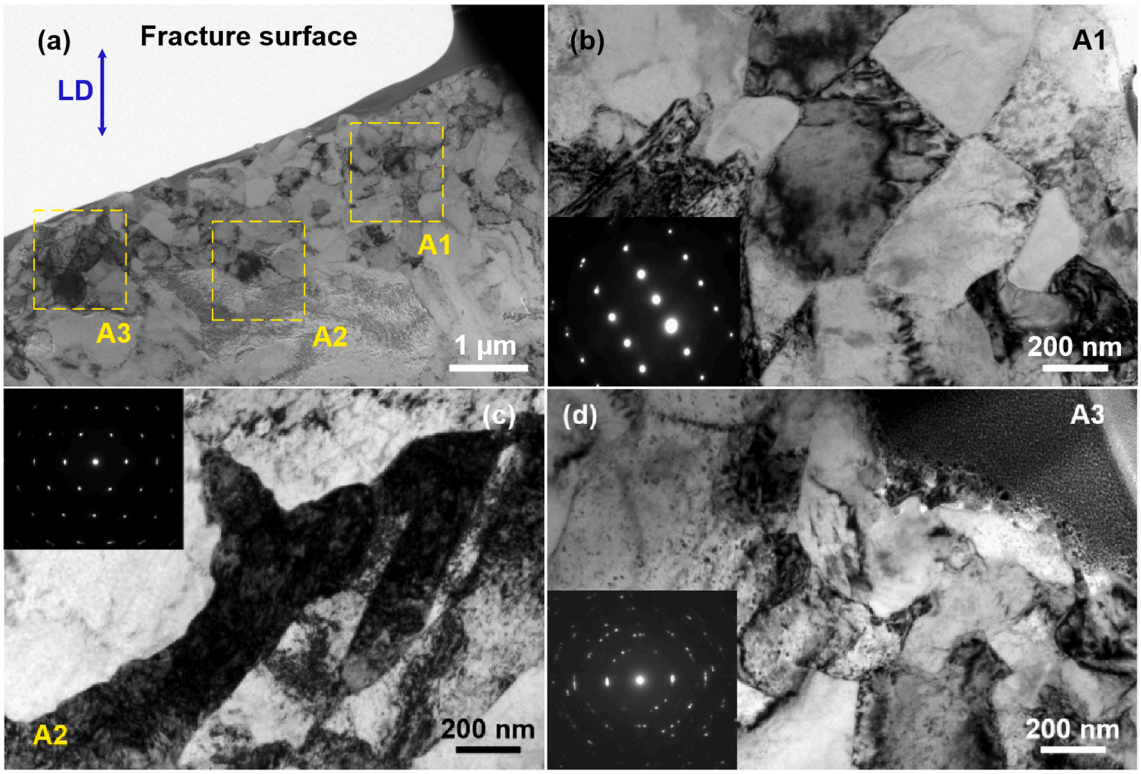

Fig. 14. TEM images showing detailed morphologies of the FIBed sample S04: (a) an overview of sub-structures below fracture surface, (b-d) are enlarged dashed areas of A1, A2 and A3, while the inserted figures in (b-d) showing results by selected area diffraction technique.

morphologies at NaCl and steam environments are shown in Figs. 3-5, where Figs. 3-4 and Fig. 5 present fracture surface morphologies at R of -1 and 0, respectively. Fig. 3a, 4a and 5a show overviews of crack initiation area with selected sub-zones for FIB milling, as depicted by yellow dashed rectangular, which are further enlarged for observation and are illustrated in Fig. 3c-e, 4b-c and 5b-e. Note that the sub-zones are labeled differently with **N**, **S**, and **S0** representing NaCl solution, and steam ($R = -1$ and 0). It is observed that the cracking mode around inclusions is not uniform, and mainly consists of transgranular and faceted modes, very similar to the fracture appearance in the near-threshold regime [33,34]. In the case of NaCl solution in Fig. 3a, the fracture surface nearby the inclusion is wavy, not flat, full of facets, implying the internal fatigue cracking process is rather complicated. It would be interesting to find the variance of FGA with the distance to inclusion, and to illustrate the possibility of fracture mode dependence of FGA formation.

3.3. Sub-structures around inclusions

Those FIBed samples at various sub-zones under different environments were characterized by a combination of TEM/SAD [26,35,36] and EBSD/TKD [15] techniques to illustrate sub-structures around inclusions and correlate with FGA formation in cases of varied distance to inclusion and fracture mode.

3.3.1. NaCl solution ($R = -1$)

Figs. 6 and 7 show microstructure morphologies below fracture surface of FIBed samples in 3% NaCl aqueous solution, corresponding to transgranular mode of fracture in N1 and N2 in Fig. 3. It is apparent the microstructures vary from fracture surface to interior depth where lathy martensites are almost intact, as observed from the overview in Fig. 6a. Interestingly, enlarged views of A1, A2 and A3 close to fracture surface in Fig. 6b-d provide clear evidence of sub-structures with dislocation cells like fine grains, which is believed to be originated from breakdown of lathy martensites. The residual lath boundaries in Fig. 6d may have implied the incomplete microstructural damage process. The dislocation cell structures are proved to be polycrystalline characteristics based on SAD analysis (the inserted figures in Fig. 6b-c), and thus inform the FGA formation in the case of VHCF fatigue under NaCl environment. A very similar microstructural morphology is shown in Fig. 7, which once again well correlates transgranular fracture mode with microstructural damage and local FGA formation.

By contrast, Fig. 8 presents microstructure morphologies beneath faceted fracture surface (sub-zone of N3 in Fig. 3e). It is interesting to find that the lathy martensites are almost intact with clear lathy martensite boundaries, and no characteristic of microstructural damage and fine grain is observed in the enlarged views of A1, A2 and A3 (Fig. 8b-d). This indicates no FGA is formed near and below the faceted fracture surface, and implies there exists a correlation of fracture mode with the occurrence of FGA. As a result, the FGA is not uniformly formed around the inclusion and is most likely fracture mode dependent.

3.3.2. Steam environment ($R = -1$)

Figs. 9 and 10 show microstructure morphologies at two sub-zones of S1 and S2 in Fig. 4, which corresponds to transgranular mode at R of -1 under steam environment. Note the S1 is closer to the inclusion than S2. It is observed from Fig. 9a that microstructure distribution is not uniform with fatigue damaged areas or intact lath martensites. The enlarged morphologies of A1, A2 and A3, as well as the SAD, illustrate sub-grains and dislocation cells in A1 (Fig. 9b), and clear lathy microstructures in A2 and A3 (Fig. 9c and d). Note A1 is much nearby the inclusion relative to A2 and A3. This further indicates the FGA formation is well represented by dislocation cells due to lath martensites breakdown. Meanwhile, dislocation cells are easier to appear on the fracture surface near inclusions due to localized plasticity, which is not unexpected.

A similar microstructure morphology is illustrated in Fig. 10 where the FIBed sample has a curved shape and accords with the fracture

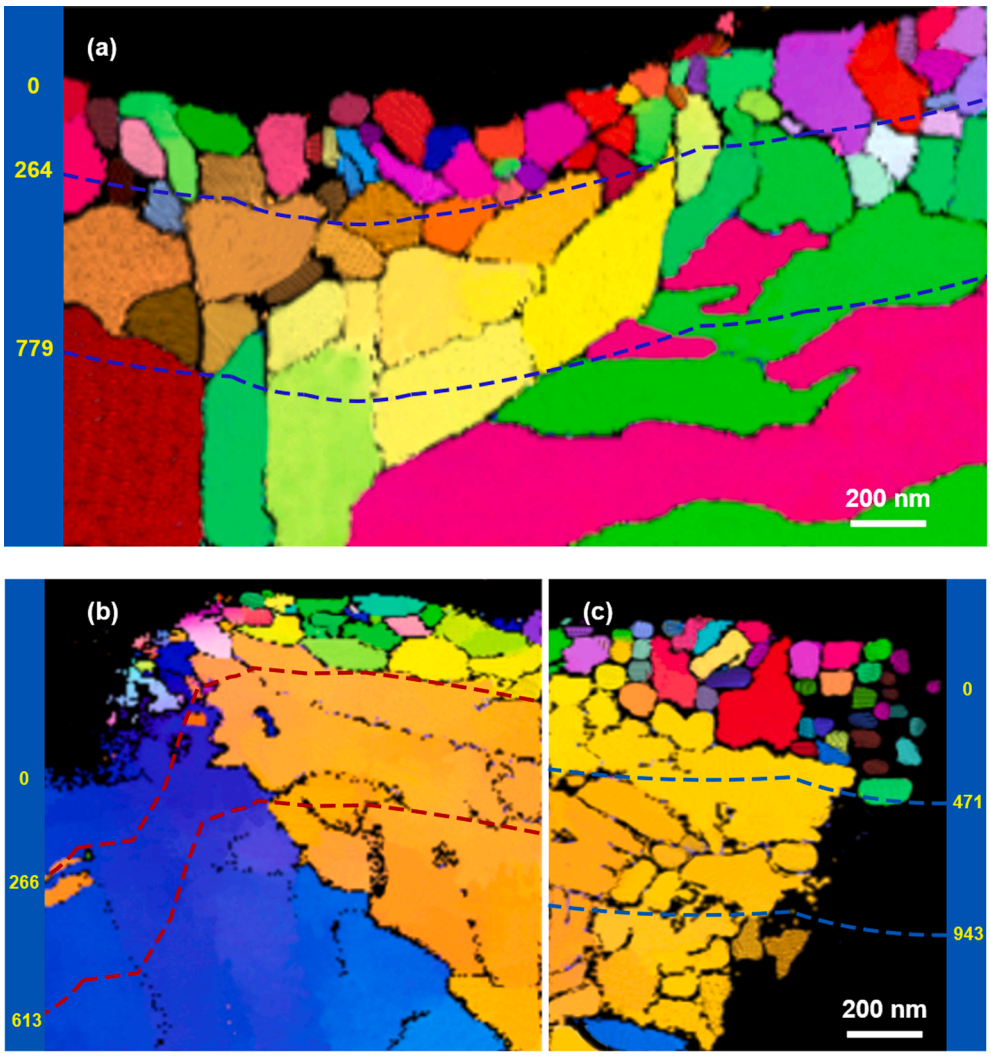

Fig. 15. EBSD images showing distribution of microstructures below fracture surfaces of FIBed samples in 3% NaCl: (a) N1, (b) N2-A1, (c) N2-A2.

surface at S2 (Fig. 4). The SAD results present the occurrence of FGA in Fig. 10b where the microstructures have complex dislocations, which shows clear difference from A2 and A3 (Fig. 10c and d) at which the martensites are observed with clear lath boundaries. It appears lath martensite fracture reflects microstructural damage in the early stage of crack initiation, and thus similar mechanisms for FGA formation are observed in steam and NaCl environments.

3.3.3. Steam environment ($R = 0$)

Figs. 11-14 show the microstructure morphologies below fracture surface at R of 0 under steam environment. The sub-zones of S01 and S03 correspond to transgranular fracture mode and close to the inclusion (Fig. 5), and detailed morphologies in Figs. 11 and 12 indicate the FGA is formed at local areas of A1 and A1/A3, respectively, where the SAD results accord well with dislocation cell sub-structures and fine grains. The sub-zone of S02 correspond to faceted fracture while the S04 has a mixed transgranular and faceted fracture mode in Fig. 5, and microstructure morphologies are shown in Figs. 13 and 14. No fine grains are observed in Fig. 13, while interestingly, a local area of A3 in Fig. 14a show the existence of FGA as evidenced by the SAD result in Fig. 14d. It is thus inferred that the FGA can be formed when R is increased from −1 to 0, and the transgranular fracture mode in S04 corresponds well with the formation of fine grains.

3.4. Distribution of fine grains

Fig. 15 shows the distribution of microstructures below fracture surfaces of FIBed samples in 3% NaCl. It presents the morphology of FGA at corresponding areas of A1, A2 and A3 in Fig. 6. Each field for EBSD scanning has a range roughly estimated as 6 μm length (radial direction) and 1 μm depth (underneath the fracture surface). As shown by the dashed lines in Fig. 15a-c, most of the fine grains have a depth of 264 nm, 266 nm and 471 nm below fracture surface, respectively. Compared with the thickness of FGA reported in open literatures, including Hong et al. [26] (500–800 nm, high strength steels), Spriestersbach et al. [37] (<200 nm, bearing steel) and Tofique et al. [38] (100–350 nm, duplex stainless steel), the current results verify an inhomogeneous distribution of FGA thickness.

The fine grain size within FGA is further analyzed to reveal the distribution in a quantitative way. In this work, a manual sizing using Image-Pro Plus 6.0 software is then performed, and statistical distribution of equivalent diameter size is illustrated in Fig. 16. It is observed in Fig. 16a that about 67% of the fine grains have equivalent diameters in the range of 50–200 nm, while almost 70% of the grains have equivalent diameters in the range of 0–150 nm in Fig. 16b-c. When analyzing the results statistically, as shown in Table 1, in the case of N1 area, the equivalent diameter ranges at 50–300 nm when it is 0–264 nm from the surface, and 200–400 nm when it is 264–779 nm away from the surface. Similar distributions can be observed in the areas of N2-A1 and N2-A2,

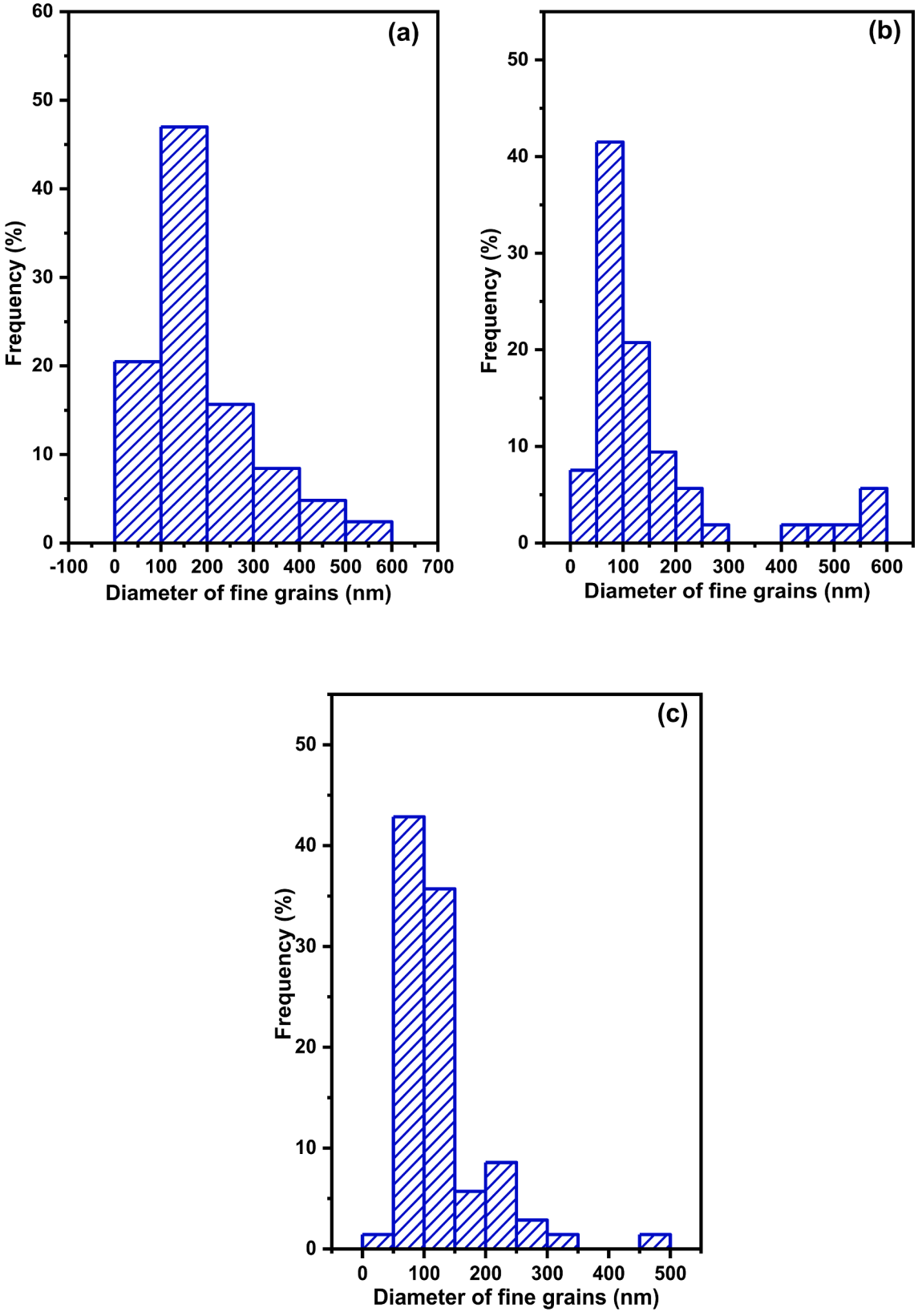

Fig. 16. The statistical distribution of equivalent diameter of fine grains: (a) N1, (b) N2-A1, (c) N2-A2.

Table 1
Quantitative analysis of grain diameter and depth of FGA layer in NaCl environment.

Area	First gradient layer (nm)	Diameter range (nm)	Probability (%)	Second gradient layer (nm)
N1	<264	<300	84	264–779
N2-A1	<266	<200	79	266–613
N2-A2	<471	<200	85	471–943
N3	No fine grains			

which further verifies the gradient distribution of fine grains below fracture surface, except for the area of N3 where faceted fracture dominates. Interestingly, the fine grain size is obviously smaller than the lath width of martensite (200–300 nm), which helps for the inference that the formation of FGA is related with the fracture of lath martensite even under environmental conditions.

3.5. Hydrogen distribution around inclusions

The ToF-SIMS analysis can provide hydrogen distribution in an area. Fig. 17 shows the 2D mapping of measurement results in the three testing conditions, where Fig. 17a, c and e present fracture surface

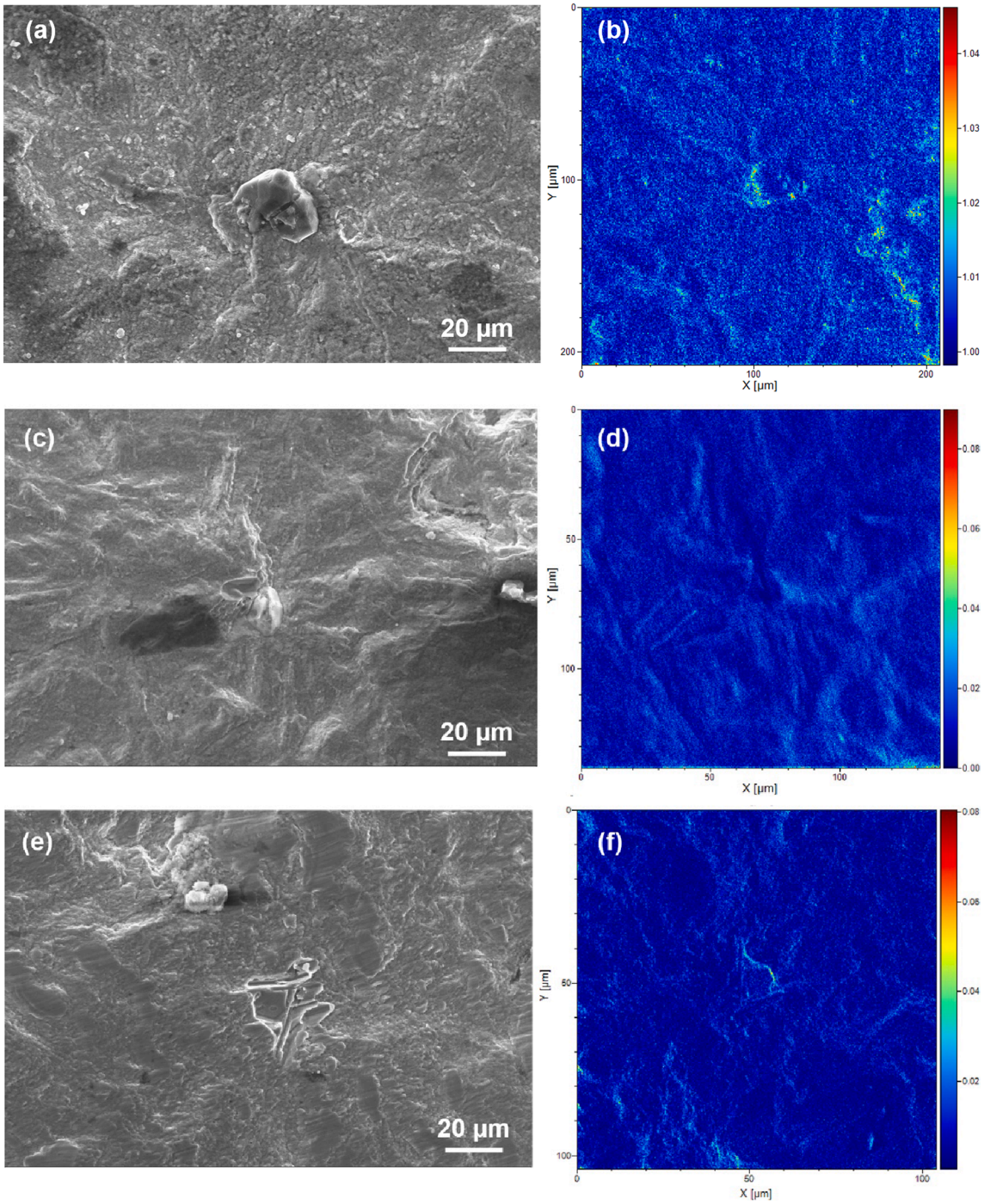

Fig. 17. Fracture morphologies (a, c, e) and hydrogen distribution nearby inclusions (b, d, f) based on SIMS analysis: (a, b) specimen in 3% NaCl ($\sigma_a = 560$ MPa, $N_f = 1.1 \times 10^7$ cycles), (c, d) specimen in steam environment ($\sigma_a = 540$ MPa, $N_f = 1.05 \times 10^7$ cycles), and (e, f) specimen in air ($\sigma_a = 525$ MPa, $N_f = 5.26 \times 10^7$ cycles).

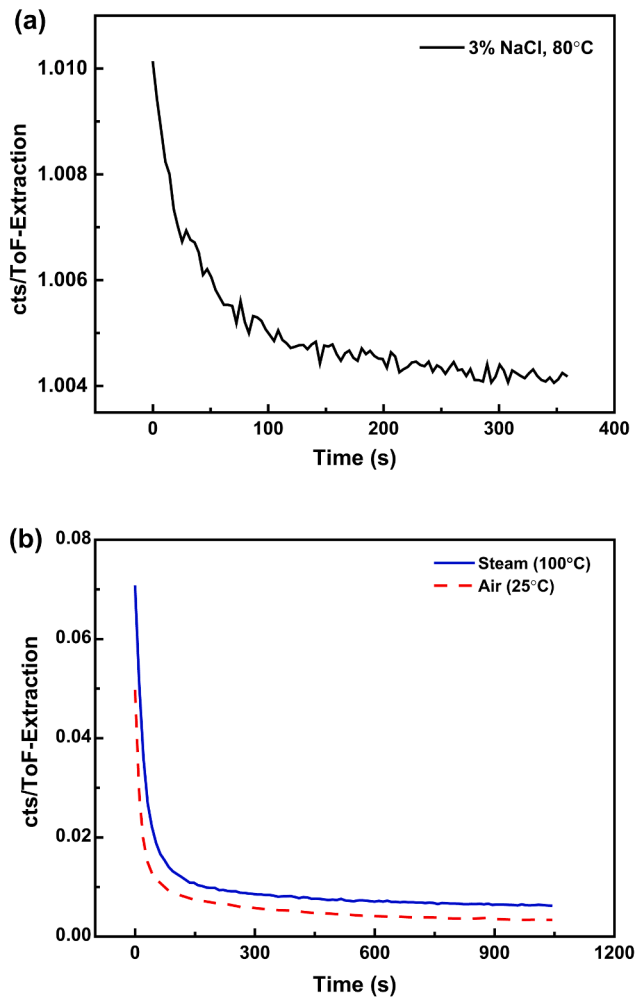

Fig. 18. Quantitative distribution of relative hydrogen content nearby micro-defect of fatigued samples in three types of testing environments: (a) 3% NaCl ($\sigma_a = 450$ MPa, $N_f = 3.77 \times 10^7$ cycles), (b) steam and air ($\sigma_a = 540$ MPa, $N_f = 1.05 \times 10^7$ cycles), air ($\sigma_a = 525$ MPa, $N_f = 5.26 \times 10^7$ cycles).

Table 2
Quantitative analysis of relative content of hydrogen in different testing environments.

Environment	Cts/ToF-Extraction
NaCl (3%, 80℃)	1.001–1.004
Steam (100℃)	0.005–0.075
Air (25℃)	0–0.005

containing critical inclusions, while Fig. 17b, e and f are the corresponding hydrogen distribution. Note the color bar on the right side of the map indicates the concentration degree of hydrogen element. It is interesting to find that the hydrogen concentration around the inclusion is higher than that in other areas, regardless of environmental media, implying a higher potential of hydrogen trapping by inclusions. A more quantitative illustration of hydrogen distribution is shown in Fig. 18, where the horizontal axis is sputtering time while the vertical axis represents counts/TOF extraction. The response value refers to the signal strength reflected when the detected element passes through the detector. As a result, the larger the response value, the higher the hydrogen concentration. It is observed in Fig. 18 that the response value decreases with time indicating an attenuation feature. Table 2 lists the response values of cts/TOF extraction in the three environments. It shows that the response values of cts/TOF extraction around inclusion is about 1.001–1.004 in 3% NaCl, 0.005–0.075 in steam, and 0–0.005 in air, that is, the content of hydrogen is the highest in 3% NaCl, followed by steam and the lowest in air. The varied hydrogen content and its influence on micro-defect induced interior fatigue cracking need to be discussed.

4. Discussion

4.1. The physics of FGA

A significant influence of environment on fatigue behavior can be observed in terms of the shape of *S-N* curves and associated fatigue strength reduction in Fig. 2 when compared with the results in air. Fatigue data for surface-initiated failures are scattered due to easy environment attack, while the data for interior micro-defect induced fatigue failures have similar slope values in various environment media. As mentioned in Section 3.1, micro-defect induced fatigue cracking has indicated intrinsic behavior of this kind of material in the VHCF regime. Note that an increase temperature of 100 °C does not soften the material, and accordingly, fatigue strength reduction in Fig. 2 is also believed to be associated with environmental attack, as evidenced by the hydrogen distribution around micro-defect, as reported in Section 3.5. As a result, hydrogen is involved in inclusion-matrix interaction during cyclic loading, and may have played important roles in microstructural damage in the VHCF regime. Murakami [23] proposed a hydrogen-assisted cracking or embrittlement as a consequence of hydrogen trapped by the inclusion as evidenced by an increased hydrogen concentration around the inclusion [39], and correlated with the formation of optically dark area (ODA) [40]. Nagao et al. [41] thought steps and ridges (like facets) on quasi-cleavage surfaces were associated with martensitic microstructure, and driven by a hydrogen-enhanced and plasticity-mediated decohesion mechanism.

Apart from the hydrogen distribution measurement, dislocation structures around critical inclusions were analyzed based on detailed characterization of microstructural damage by FIB and TEM techniques. Dislocation cells can be obviously observed around lathy martensites in Fig. 19a, and the size of them are comparable to fine grains in Fig. 19b with the help of BSE imaging technique. Fig. 19c shows an enlarged view of microstructures in Fig. 19a, indicating the distribution of lathy martensites and those dislocation nanostructures around, where a large number of low energy dislocation nanostructures can be observed more clearly. Interestingly, it has been confirmed the formation of low energy dislocation nanostructures is related to hydrogen in a BCC structural material [42]. Upon deformation in a hydrogen-rich environment, microstructures displayed enhanced dislocation mobility and serious dislocation-precipitate interactions, consequently fostering the formation of low-energy dislocation nanostructures. In addition, Nygren et al. [43] indicated that internal hydrogen affected microstructural evolution, resulting in the formation of smaller dislocation cells with thicker cell walls in a FCC material, in terms of the hydrogen-enhanced localized plasticity (HELP). Another enlarged view of microstructures is shown in Fig. 19d, where a large number of dislocations bow out from the lath interface, such kind of lath-dislocation morphology supports the mechanism of “fragmentation of martensitic laths and formation of dislocation cells” [15]. In addition, it is observed that the boundary of fine grains under environment is clearer than that in air. Therefore, it can be concluded that hydrogen contributes to the formation of low energy dislocations, and thus speedup breakdown of lath martensites. Under this scenario, the cyclic number or crack initiation life consumed in the formation of FGA is shortened in the case of hydrogen contribution, which accordingly shortens total fatigue life under environment, by comparing with that in air at the same loading level. All these helps clarify the contribution of hydrogen to internal cracking, based on which the lower fatigue strength under environment media is rationalized.

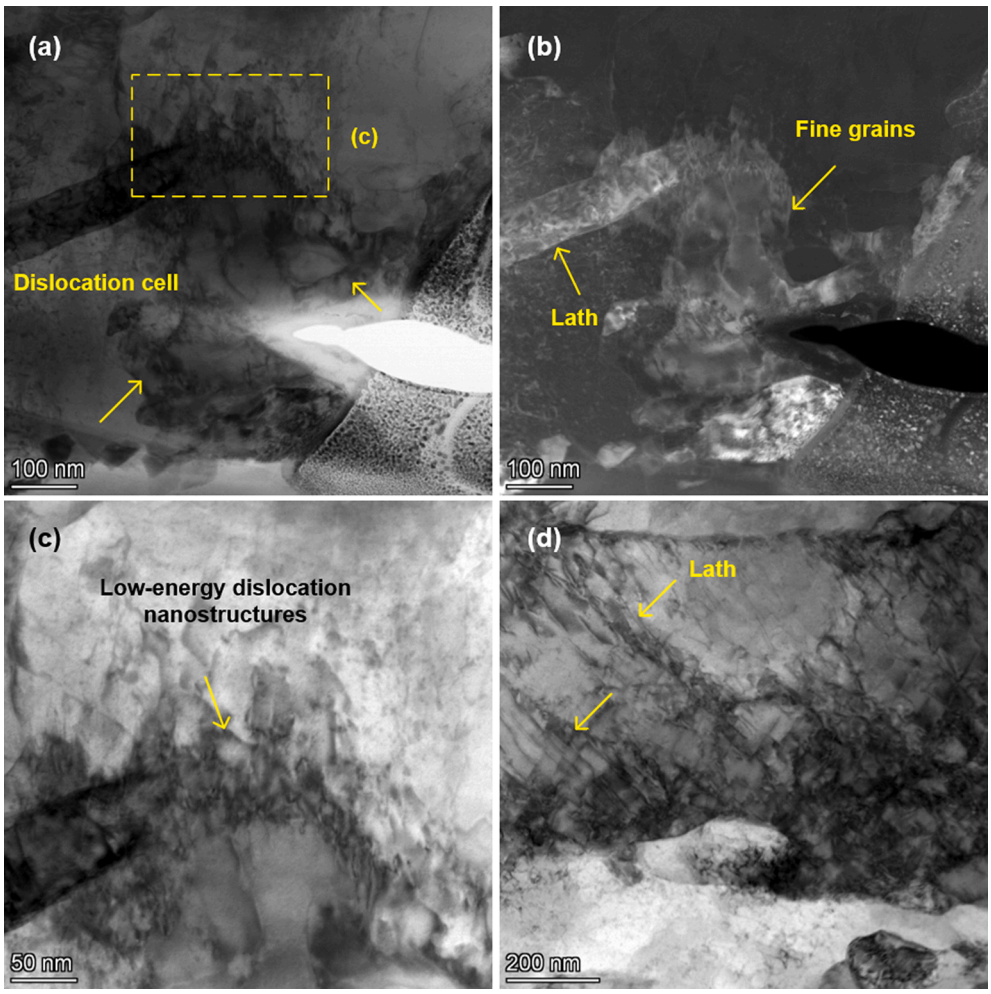

Fig. 19. STEM images showing microstructure morphologies of specimen at steam environment under $R = -1$ ($\sigma_a = 420$ MPa, $N_f = 9.42 \times 10^7$ cycles): (a) formation of dislocation cells, (b) BSE image of dislocation cell, (c) magnified morphologies in (a), and (d) dislocations bow out from the lath interface.

Table 3
Parameters for calculation of FGA under three environments.

Environment	Stress ratio (R)	Stress amplitude (MPa)	Fatigue life (cycle)	$\sqrt{area}_{inc}$(μm)	t_{FGA} (nm)	ΔK_{FGA} (MPa·m$^{1/2}$)
air	−1	575	2.20×10^7	11.23	800	3.53
NaCl	−1	525	1.68×10^7	12.68	779	3.41
NaCl	−1	525	1.68×10^7	12.68	613	3.39
NaCl	−1	525	1.68×10^7	12.68	943	3.43
Steam	−1	520	1.12×10^7	12.89	581	3.38
Steam	−1	420	9.42×10^7	16.60	420	3.07
Steam	0	440	1.38×10^7	14.21	797	3.02
Steam	0	440	1.38×10^7	14.21	695	3.01
Steam	0	440	1.38×10^7	14.21	587	3.00

4.2. The mechanics of interior fatigue cracking

Whether the formation of FGA belongs to crack initiation or propagation stage is still an open issue, while Zhu et al. [15] claimed the FGA was a crack initiation and early propagation process. *In this work, an assumption of crack propagation is firstly made, on which the interior cracking behavior is thus discussed by classic fracture mechanics.* Note the size of micro-defect (10–100 μm) is larger than the width of martensite lath (200–300 nm), and thus the interior inclusion can be regarded as a physically short crack, at which the theory of elastic plastic fracture mechanics is applicable [44]. In this case, the mechanics of FGA have two conditions to be satisfied: (i) the cyclic plastic zone has been developed around micro-defect, with its size no less than FGA size, i.e., $a_{FGA} \leqslant r_{pc}$; (ii) the instant stress intensity factor (SIF) range at FGA does not exceed fatigue threshold of long fatigue crack, ΔK_{th}, i.e., $\Delta K_{inc} \leqslant \Delta K_{FGA} \leqslant \Delta K_{th}$.

By taking the Mises criterion for yielding, the monotonic plastic zone size (r_p) under plane strain condition under mode-I crack loading are derived as a function of θ, as shown in Eq. (1). When $\theta = 0°$, the cyclic plastic zone size (r_{pc}) around micro-defect in crack propagation direction is thus calculated to be Eq. (2).

$$r_p(\theta) = \frac{1}{4\pi}\left(\frac{K_I}{\sigma_y}\right)^2 \left(\frac{3}{2}sin^2\theta + (1 + cos\theta)(1 - 2\nu)^2\right) \quad (1)$$

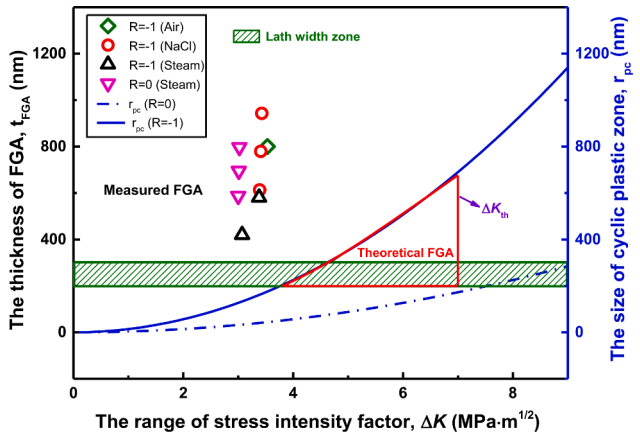

Fig. 20. Variations of FGA thickness and cyclic plastic zone with stress intensity factor range.

$$r_{pc} = \frac{1}{8\pi}\left(\frac{\Delta K_{inc}}{\sigma_y}\right)^2(1-2\nu)^2 \tag{2}$$

According to Irwin's crack length correction, an effective crack length for FGA, a_{FGA}, is corrected by the thickness of nanocrystalline layer, t_{FGA}, as shown in Eq. (3), where $\sqrt{area}_{inc}$ is the inclusion size.

$$a_{FGA} = \sqrt{area_{inc}} + t_{FGA} \tag{3}$$

With $K = Y\sigma\sqrt{\pi a}$, the size of theoretical FGA zone is established as,

$$a_{FGA} = \frac{1}{\pi}\left(\frac{\Delta K_{FGA}}{Y\Delta\sigma}\right)^2 = \frac{1}{4\pi}\left(\frac{\Delta K_{FGA}}{Y\sigma_a}\right)^2 \tag{4}$$

where, Y is shape factor, and σ_a is stress amplitude.

In this work, a new parameter, z, is defined as the ratio of cyclic plastic zone to theoretical FGA size, as shown in Eq. (5), and taken as a verification parameter for the interior cracking mechanics.

$$z = \frac{r_{pc}}{a_{FGA}} = \frac{\frac{1}{8\pi}\left(\frac{\Delta K_{inc}}{\sigma_y}\right)^2(1-2\nu)^2}{\frac{1}{4\pi}\left(\frac{\Delta K_{FGA}}{Y\sigma_a}\right)^2} = \frac{1}{2}Y^2(1-2\nu)^2\left(\frac{\sigma_a}{\sigma_y}\right)^2\cdot\left(\frac{\Delta K_{inc}}{\Delta K_{FGA}}\right)^2 < 1 \tag{5}$$

It is observed from Eq. (5) that, the size of cyclic plastic zone cannot exceed the theoretical FGA size, i.e., z is below one. Note that the σ_y can be higher with hydrogen contribution. *This verifies the assumption of crack propagation is inappropriate for FGA, and thus provides the evidence that the formation of FGA is not by crack propagation.*

A further verification is made by making quantitative analysis of FGA thickness. Note the FGAs at fracture surfaces near micro-defect of failed specimens were detected with TEM and measured by Image Pro Plus. The TEM blocks extracted from FGAs by FIB were sampled in radial direction to characterize microstructural change inside the FGA. In the case of circular crack propagation, the FGA thickness can be measured at different FGA crack length, as a result, t_{FGA} was measured on TEM images at different positions. Therefore, this allows the calculation of SIF for each measuring position for subsurface cracks.

By taking $Y = 0.5$ for internal cracking [45], the FGA size and the SIF at crack tip can be determined as a function of crack length according to Eqs. (2) and (3). Note that ΔK_{FGA} is approaching the fatigue threshold of long cracks, ΔK_{th}, at which the final FGA is formed. Zhu et al. [46] reported that the ΔK_{th} was about 6.8 MPam$^{1/2}$ at $R = 0.1$ in a similar lath martensitic steel, in addition, the ΔK_{th} could have apparent increase when R is decreased due to significant effect of crack closure [47,48]. The raw data and calculation results of FGA are listed in Table 3, and a quantitative comparison is illustrated in Fig. 20. It is observed that the measured FGA size is much larger than the calculated cyclic plastic zone size, which further confirms the claim that FGA is not formed by crack growth. As normally known that the cyclic plasticity is mainly driven by stress amplitude which can be reduced with increasing R. This would reduce cyclic plasticity localization around micro-defect and a lower probability of FGA formation. This indicates the FGA is more difficult to form with the increasing of R, as has been widely reported [49].

4.3. Chemo-mechanical model of interior cracking

Fatigue cracking in the case of micro-defect has both mechanical and environmental factors involved. In terms of fatigue cracking under hydrogen effect, the hydrogen-enhanced localized plasticity (HELP) mechanism may occur with hydrogen-enhanced decohesion (HEDE) mechanism in a sequential manner. The HELP mechanism is associated

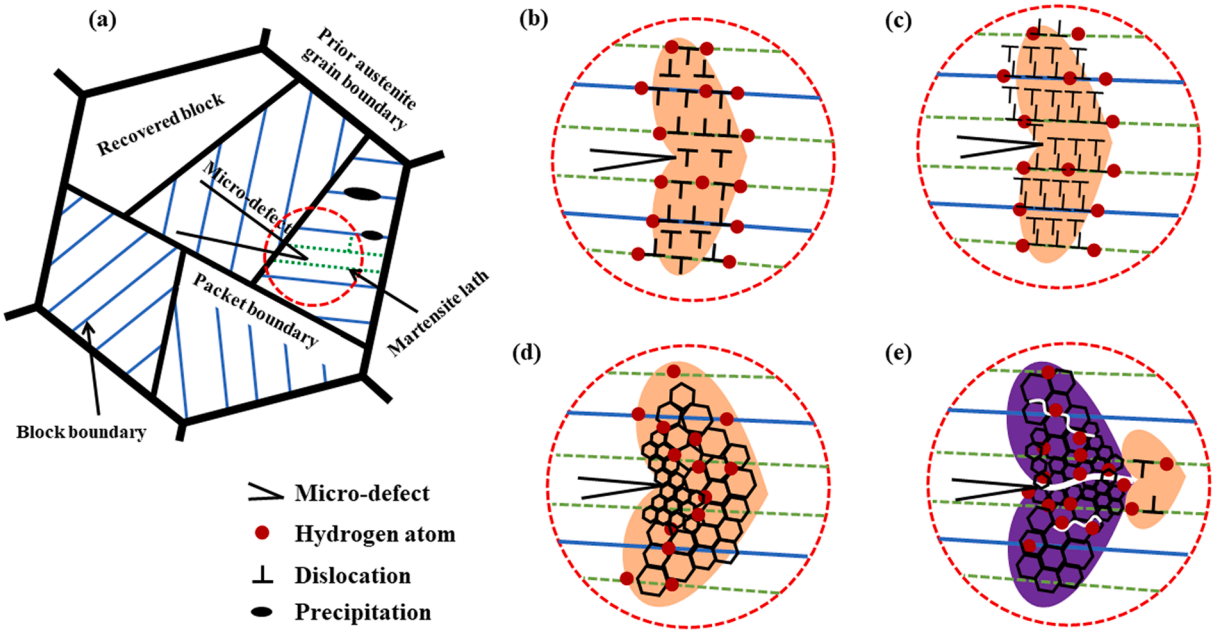

Fig. 21. Mechanistic modeling of FGA formation: (a) schematic of prior austenite grain with its constituents clearly represented, (b) hydrogen atom and dislocation motion within local plastic area, (c) dislocation multiplication and dislocation cells formation inside plastic volume, (d) subgrain boundaries built from dislocation cells, (e) crack initiation and propagation in fine granular volume.

with microstructural refinement into dislocation cell structures and extensive plasticity in the form of intense slip bands, while the activation of HEDE was assisted by the HELP mechanism, as claimed by Nagao et al. [41,50]. Typical hydrogen traps include block and lath boundaries, carbides, inclusions, and prior austenite grain boundaries in lathy martensitic steels. In this work, based on a thorough examination of interior micro-defect induced fatigue cracking, a chemo-mechanical model is thus proposed on the basis of previous FGA models [15,25,36,51,52].

Fig. 21 is a schematic illustration of four steps for formation of FGA. Fig. 21a represents several microstructural elements in a lathy martensite steel. The localized plasticity around micro-defect promotes hydrogen diffusion, in return, for an enhanced local plasticity. Under cyclic loading, dislocations move frequently, and even to lathy boundaries where hydrogen atoms trapped, as shown in Fig. 21b. The hydrogen-dislocation interaction results in high density of dislocations, and subsequently with increasing lifetime, as exhibited in Fig. 21c, dislocations develop an energetically favorable state in the form of dislocation cells with thick cell walls with the help of hydrogen [42]. This is followed by subgrain boundaries formation in the small plastic volume inside the martensitic lath by dislocation annihilation to minimize the local elastic energy, as shown in Fig. 21d. The initial martensitic lath will be refined into fine grains, which has been well described in the previous model by Zhu et al. [15]. This clearly shows a crack initiation process in terms of microstructural damage due to chemo-mechanical interaction.

As reported widely [53,54], the threshold value for crack propagation decreases with decreasing grain size. Thus, local threshold value ΔK_{th} can be lowered due to local grain refinement, implying an easier crack propagation. As shown in Fig. 21e, the micro-cracks at fine grain boundaries or interfaces, probably driven by HEDE mechanism [55], can coalescence with each other, and propagate through the refined volume. With early extension of the originated crack, the repeated pressing at crack wake further helps grain refinement. Meanwhile, crack-tip plasticity is gradually developed until FGA is finally formed. This provides a rationalization for early growth feature of FGA formation.

Therefore, it is the interactions of inclusion, matrix, and environment, that drive the formation of FGA. This is an extension of the previous matrix-inclusion scenario, and a further verification of FGA formation in terms of microstructural damage, indicating the significance of "fragmentation of martensitic laths and formation of dislocation cells" in the physics of micro-defect induced fatigue cracking. In addition, the current chemo-mechanical model of interior cracking, is more or less believed as a general damage model, which extends the mechanism to environmental conditions, and most importantly, provides a practical connection and thus unification of the hydrogen assisted fatigue cracking proposed by Murakami [23] 20 years ago.

5. Conclusions

Axially cyclic tests of one precipitation-hardened martensitic steel in 3% salt water (80℃) and steam (100℃) with $R = -1$ and 0 were carried out to investigate the interior micro-defects induced cracking in the HCF and VHCF regimes. A significant number of experiments as well as theoretical modeling was carried out to illustrate the physics and mechanics of micro-defect induced interior cracking for a general fatigue damage law. The main conclusions are listed as follows.

(1) There existed apparent environmental effect on fatigue behavior as evidenced by more scattered data points in short life regime ($\leq 5\times10^6$) and decreased fatigue strength relative to air environment up to the VHCF regime.
(2) The FGA was also formed in environmental media, heterogeneously distributed around micro-defect, and was found dependent on local fracture mode with a less probability in the case of faceted failure, as a result of "fragmentation of martensitic laths and formation of dislocation cells" under hydrogen influence as verified by the low energy dislocation nanostructure around inclusion.
(3) The formation of FGA would not be induced by crack propagation but driven by microstructural damage with contribution from cyclic loading, as confirmed by both theoretical modeling and FGA thickness measurement, and by comparison with microstructural and cyclic plastic zone size.
(4) A general fatigue damage law for interior micro-defect induced cracking should obey the scenario of interactions of inclusion, matrix, and environment, on which a *chemo-mechanical model of interior cracking* was established with hydrogen contribution properly represented, which was expected to connect and thus unify Murakami model [23] and Zhu's model [15].

Declaration of Competing Interest

The authors declare that they have no known competing financial interests or personal relationships that could have appeared to influence the work reported in this paper.

Acknowledgements

The authors are grateful for the supports provided by the National Natural Science Foundation of China (51922041, 51835003).

References

[1] Zerbst U, Klinger C. Material defects as cause for the fatigue failure of metallic components. Int. J. Fatigue 2019;127:312–23.
[2] Murakami Y. High and ultrahigh cycle fatigue. Comp. Struct. Integ. 2003;4:41–76.
[3] Nishida, Shin-ichi, Failure Analysis in Engineering Applications, 1992, pp. 6–21.
[4] Wang QY, Bathias C, Kawagoishi N, Chen Q. Effect of inclusion on subsurface crack initiation and gigacycle fatigue strength. Int. J. Fatigue 2002;24:1269–74.
[5] Wagner D, Ranc N, Bathias C, Paris PC. Fatigue crack initiation detection by an infrared thermography method. Fatigue Fract. Eng. Mater. Struct. 2010;33:12–21.
[6] Stanzl-Tschegg SE, Schoenbauer B. Mechanisms of strain localization, crack initiation and fracture of polycrystalline copper in the VHCF regime. Int. J. Fatigue 2010;32:886–93.
[7] Li SX. Effects of inclusions on very high cycle fatigue properties of high strength steels. Int. Mater. Rev. 2012;57:92–114.
[8] Pineau A, Antolovich SD. Probabilistic approaches to fatigue with special emphasis on initiation from inclusions. Int. J. Fatigue 2016;93:422–34.
[9] Sakai T, Oguma N, Morikawa A. Microscopic and nanoscopic observations of metallurgical structures around inclusions at interior crack initiation site for a bearing steel in very high-cycle fatigue. Fatigue Fract. Eng. Mater. Struct. 2015;38:1305–14.
[10] Awd M, Siddique S, Johannsen J, Emmelmann C, Walther F. Very high-cycle fatigue properties and microstructural damage mechanisms of selective laser melted AlSi10Mg alloy. Int. J. Fatigue 2019;124:55–69.
[11] Hong Y, Lei Z, Sun C, Zhao A. Propensities of crack interior initiation and early growth for very-high-cycle fatigue of high strength steels. Int. J. Fatigue 2014;58:144–51.
[12] Abdesselam H, Crepin J, Pineau A, Rouffie AL, Gaborit P, Menut-Toumadre L, et al. On the crystallographic, stage I-like, character of fine granular area formation in internal fish-eye fatigue cracks. Int. J. Fatigue 2018;106:132–42.
[13] Janssen MHE, Hermans MJM, Janssen M, Richardson IM. Fatigue properties of laser-brazed joints of Dual Phase and TRansformation Induced Plasticity steel with a copper-aluminium consumable. Mater. Des. 2010;31:3922–8.
[14] Dunstan MK, Paramore JD, Fang ZZ. The effects of microstructure and porosity on the competing fatigue failure mechanisms in powder metallurgy Ti-6Al-4V. Int. J. Fatigue 2018;116:584–91.
[15] Zhu M-L, Jin L, Xuan F-Z. Fatigue life and mechanistic modeling of interior micro-defect induced cracking in high cycle and very high cycle regimes. Acta Mater. 2018;157:259–75.
[16] Matsunaga H, Sun C, Hong Y, Murakami Y. Dominant factors for very-high-cycle fatigue of high-strength steels and a new design method for components. Fatigue Fract. Eng. Mater. Struct. 2015;38:1274–84.
[17] Murakami Y, Nomoto T, Ueda T, Murakami Y. On the mechanism of fatigue failure in the superlong life regime (N > 10(7) cycles). Part II: a fractographic investigation. Fatigue Fract. Eng. Mater. Struct. 2000;23:903–10.
[18] Sakai T, Sato Y, Oguma N. Characteristic S-N properties of high-carbon-chromium-bearing steel under axial loading in long-life fatigue. Fatigue Fract. Eng. Mater. Struct. 2002;25:765–73.
[19] Lei Z, Xie J, Sun C, Hong Y. Effects of loading condition on very-high-cycle fatigue behaviour and dominant variable analysis. Sci. China-Phys. Mech. Astron. 2014;57:74–82.

[20] Shyam A, Blau P, Jordan T, Yang N. Effect of submillimeter size holes on the fatigue limit of a high strength tool steel. Fatigue Fract. Eng. Mater. Struct. 2014; 37:368–79.
[21] Sun C, Liu X, Hong Y. A two-parameter model to predict fatigue life of high-strength steels in a very high cycle fatigue regime. Acta Mech. Sin. 2015;31: 383–91.
[22] Shiozawa K, Lu L, Ishihara S. S-N curve characteristics and subsurface crack initiation behaviour in ultra-long life fatigue of a high carbon-chromium bearing steel. Fatigue Fract. Eng. Mater. Struct. 2001;24:781–90.
[23] Murakami Y, Nomoto T, Ueda T, Murakami Y. On the mechanism of fatigue failure in the superlong life regime (N > 10(7) cycles). Part I: influence of hydrogen trapped by inclusions. Fatigue Fract. Eng. Mater. Struct. 2000;23:893–902.
[24] Sakai T, Takeda M, Tanaka N, Kanemitsu M, Shiozawa K. S-N Property and Fractography of High Carbon Chromium Bearing Steel over Ultra Wide Life Region under Rotating Bending. Nihon Kikai Gakkai Ronbunshu, A Hen/Trans. Jpn. Soc. Mech. Eng., Part A 2001;67:1805–12.
[25] Grad P, Reuscher B, Brodyanski A, Kopnarski M, Kerscher E. Mechanism of fatigue crack initiation and propagation in the very high cycle fatigue regime of high-strength steels. Scr. Mater. 2012;67:838–41.
[26] Hong Y, Liu X, Lei Z, Sun C. The formation mechanism of characteristic region at crack initiation for very-high-cycle fatigue of high-strength steels. Int. J. Fatigue 2016;89:108–18.
[27] T. Nakamura, H. Oguma, Y. Shinohara, The effect of vacuum-like environment inside sub-surface fatigue crack on the formation of ODA fracture surface in high strength steel, in: P. Lukas (Ed.), Fatigue, vol. 2010, 2010, pp. 2121–2129.
[28] Stinville JC, Martin E, Karadge M, Ismonov S, Soare M, Hanlon T, et al. Fatigue deformation in a polycrystalline nickel base superalloy at intermediate and high temperature: Competing failure modes. Acta Mater. 2018;152:16–33.
[29] Cervellon A, Hémery S, Kürnsteiner P, Gault B, Kontis P, Cormier J. Crack initiation mechanisms during very high cycle fatigue of Ni-based single crystal superalloys at high temperature. Acta Mater. 2020;188:131–44.
[30] Li W, Sun R, Hu T, Li X, Li C, Zhang Y, et al. Effect of elevated temperature on high-cycle and very-high-cycle fatigue properties of Ni-based superalloy manufactured by selective laser melting. Int. J. Fatigue 2021;148:106250.
[31] Qian G, Zhou C, Hong Y. Experimental and theoretical investigation of environmental media on very-high-cycle fatigue behavior for a structural steel. Acta Mater. 2011;59:1321–7.
[32] Sakai T, Sato Y, Nagano Y, Takeda M, Oguma N. Effect of stress ratio on long life fatigue behavior of high carbon chromium bearing steel under axial loading. Int. J. Fatigue 2006;28:1547–54.
[33] Zhu M-L, Xuan F-Z. Effect of microstructure on appearance of near-threshold fatigue fracture in Cr-Mo-V steel. Int. J. Fract. 2009;159:111–20.
[34] Du Y-N, Zhu M-L, Xuan F-Z. Transitional behavior of fatigue crack growth in welded joint of 25Cr2Ni2MoV steel. Eng. Fract. Mech. 2015;144:1–15.
[35] Zhu M-L, Xuan F-Z. Failure mechanisms and fatigue strength assessment of a low strength Cr−Ni−Mo−V steel welded joint: Coupled frequency and size effects. Mech. Mater. 2016;100:198–208.
[36] Chai G, Zhou N, Ciurea S, Andersson M, Lin Peng R. Local plasticity exhaustion in a very high cycle fatigue regime. Scripta Materialia 2012;66:769–72.
[37] Spriestersbach D, Brodyanski A, Loesch J, Kopnarski M, Kerscher E. Very high cycle fatigue of bearing steels with artificial defects in vacuum. Mater. Sci. Technol. 2016;32:1111–8.
[38] Tofique MW, Bergstrom J, Svensson K. Very high cycle fatigue of cold rolled stainless steels, crack initiation and formation of the fine granular area. Int. J. Fatigue 2017;100:238–50.
[39] Murakami Y, Matsunaga H. The effect of hydrogen on fatigue properties of steels used for fuel cell system. Int. J. Fatigue 2006;28:1509–20.
[40] Murakami Y, Yokoyama NN, Nagata J. Mechanism of fatigue failure in ultralong life regime. Fatigue Fract. Eng. Mater. Struct. 2002;25:735–46.
[41] Nagao A, Smith CD, Dadfarnia M, Sofronis P, Robertson IM. The role of hydrogen in hydrogen embrittlement fracture of lath martensitic steel. Acta Mater. 2012;60: 5182–9.
[42] Gong P, Nutter J, Rivera-Diaz-Del-Castillo P, Rainforth W. Hydrogen embrittlement through the formation of low-energy dislocation nanostructures in nanoprecipitation-strengthened steels. Sci. Adv. 2020;6:eabb6152.
[43] Nygren K, Nagao A, Wang S, Sofronis P, Robertson I. Influence of internal hydrogen content on the evolved microstructure beneath fatigue striations in 316L austenitic stainless steel. Acta Mater. 2021;213:116957.
[44] McDowell DL, Dunne FPE. Microstructure-sensitive computational modeling of fatigue crack formation. Int. J. Fatigue 2010;32:1521–42.
[45] Murakami Y. Metal Fatigue: Effects of Small Defects and Nonmetallic Inclusions. Elsevier; 2002.
[46] Zhu M-L, Xuan F-Z, Tu S-T. Interpreting load ratio dependence of near-threshold fatigue crack growth by a new crack closure model. Int. J. Press. Vessels Pip. 2013; 110:9–13.
[47] Kwofie S, Zhu M-L. Modeling R-dependence of near-threshold fatigue crack growth by combining crack closure and exponential mean stress model. Int. J. Fatigue 2019;122:93–105.
[48] Zhu M-L, Xuan F-Z, Tu S-T. Effect of load ratio on fatigue crack growth in the near-threshold regime: a literature review, and a combined crack closure and driving force approach. Eng. Fract. Mech. 2015;141:57–77.
[49] Kovacs S, Beck T, Singheiser L. Influence of mean stresses on fatigue life and damage of a turbine blade steel in the VHCF-regime. Int. J. Fatigue 2013;49:90–9.
[50] Nagao A, Dadfarnia M, Somerday BP, Sofronis P, Ritchie RO. Hydrogen-enhanced-plasticity mediated decohesion for hydrogen-induced intergranular and "quasi-cleavage" fracture of lath martensitic steels. J. Mech. Phys. Solids 2018;112: 403–30.
[51] Hong Y, Sun C. The nature and the mechanism of crack initiation and early growth for very-high-cycle fatigue of metallic materials – an overview. Theor. Appl. Fract. Mech. 2017;92:331–50.
[52] Murakami Y, Nomoto T, Ueda T. Factors influencing the mechanism of superlong fatigue failure in steels. Fatigue Fract. Eng. Mater. Struct. (Print) 1999;22:581–90.
[53] Mughrabi H, Hppel HW. Cyclic deformation and fatigue properties of very fine-grained metals and alloys. Int. J. Fatigue 2010;32:1413–27.
[54] Hockauf K, Halle T, Hockauf M, Wagner MFX, Lampke T. Near-threshold fatigue crack propagation in an ECAP-processed ultrafine-grained aluminium alloy. Mater. Sci. Forum 2010;667–669:873–8.
[55] Novak P, Yuan R, Somerday BP, Sofronis P, Ritchie RO. A statistical, physical-based, micro-mechanical model of hydrogen-induced intergranular fracture in steel. J. Mech. Phys. Solids 2010;58:206–26.